Communications: SIF Congress 2020

Small-scale magnetic reconnection during flux emergence in active regions observed in the solar atmosphere

S. L. Guglielmino

INAF, Osservatorio Astrofisico di Catania - Via S. Sofia 78, I-95123 Catania, Italy

Summary. — Magnetic reconnection is a fundamental physical process that is thought to occur in a variety of astrophysical environments, appearing to be responsible for sudden energy release phenomena. A plethora of small-scale energetic events have been discovered in the solar atmosphere, most of them linked to magnetic reconnection episodes. Here, we report on the late phases of a reconnection event, which led to the appearance of a long-lasting ultraviolet burst with coronal signatures, observed during flux emergence in the plage of an active region. In particular, we study the final jet ejections and violent eruptions, resembling mini-CMEs.

1. – Introduction

Our understanding of the solar magnetism has improved over the last years thanks to high-resolution observations and numerical models. It is widely accepted that a dynamo action occurring in the Sun generates magnetic fields by converting kinetic energy into magnetic energy [1]. This mechanism leads to the formation of magnetic flux tubes or flux ropes that are embedded in the convective zone, which can buoyantly rise through the outer solar interior [2, 3]. As a consequence, the magnetic field emerges into the solar surface and permeates the solar atmosphere, giving rise to a plethora of magnetic structures. The above-described process is known as *magnetic flux emergence.*

Emerging flux regions (EFRs) define the totality of observable phenomena from the photosphere to the corona due to magnetic flux emergence through the solar atmosphere [4]. EFRs range over several spatial and time scales, from large-scale flux concentrations, like active regions (ARs) consisting of sunspots with their umbrae and penumbrae [5], evolving along several weeks, to small-scale, sub-arcseconds[^1] flux patches observed in the quiet Sun [6], at the limit of current observational capabilities, characterized by a short-term evolution (minutes). It is still unclear if these small-scale

---

[^1]: $1'' = 725$ km on the solar disk.

solar features are the result of global or local dynamos and if they play a role in the coronal heating problem.

Long-duration, seeing-free observing sequences provided by satellites like the Hinode [7] and the Solar Dynamics Observatory (SDO, [8]) have shown that small-size EFRs populate the solar surface at every instant. During the past decade, this investigation also benefited from observations of the photosphere taken by the Imaging Magnetograph eXperiment (IMaX, [9]) aboard the Sunrise observatory [10-12]. Thanks to its high spatial resolution ($< 0.\!\!''3$) and polarimetric sensitivity, IMaX provided new information about the evolution of small-scale magnetic features, enriching the picture of the dynamic processes that occur in EFRs and providing evidence for emergence of small loops and flux sheets [13-16] and spatially resolved magnetic flux tubes [17, 18].

However, observations provided by the Sunrise Filter Imager [19] instrument, which were simultaneous and cospatial to the IMaX measurements, allowed only the middle cromospheric level to be explored by using Ca II H filtergrams. Therefore, only limited information could be obtained about the interaction of small-scale EFRs and their role in energizing the upper atmospheric layers of the Sun, investigating the chromospheric response to flux emergence [20] and flux cancellation [21].

The recent advent of the Interface Region Imaging Spectrograph (IRIS, [22]) satellite has further extended our insight into the phenomena that occur in the solar atmosphere —upper chromosphere and transition region— in response to flux emergence events. Indeed, IRIS multi-wavelength ultraviolet (UV) observations revealed unexpected complexity at these atmospheric levels. Taking advantage of a spatial resolution ($\approx 0.\!\!''35$) in the UV similar to that achieved by IMaX in the photosphere, IRIS shed light on a number of the small-scale energy release episodes, such as explosive events [23-25] and penumbral jets and brightenings [26-30]. In this context, UV bursts have been observed [31]. These are transient events (about 5 minutes) that show in UV spectra an increase of about a factor of 100–1000 in intensity and plasma flows of 100–200 $\mathrm{km\,s^{-1}}$. They occur on spatial scales of ~ 0.5 Mm and are thought to take place at low atmospheric heights. The properties of UV bursts have been assessed by [32], gathering the results coming from several observational studies [31, 33-39].

These phenomena appear to be caused by small-scale magnetic reconnection episodes. *Magnetic reconnection* is a fundamental plasma physics process that occurs at the boundary layer between opposite polarity magnetic domains. It is able to rearrange the field topology, converting magnetic energy to thermal energy, kinetic energy and particle acceleration [40]. In the Sun, the large-scale manifestation of reconnection is represented by flares [41]. At small scale, it is recognized in the presence at the photospheric level of opposite magnetic polarities that come into contact and cancel with each other, with concurrence of transient brightening and jet-like ejections in the upper layers [42].

In particular, reconnection may occur when EFRs interact with the overlying, pre-existing field lines, triggering high-temperature localized emission and driving high-speed plasma flows [43]. Such a scenario has been reported in detailed high-resolution multi-wavelength observations of small-scale EFRs, analyzing the chromospheric and coronal phenomena taking place at the emergence sites [20, 44-52].

Numerical simulations of magnetic flux emergence in the solar atmosphere support this scenario. Since the early calculations [53], models show that small-scale energy release episodes occur ubiquitously in the emergence sites, as a result of magnetic reconnection, either due to the interaction of the emerging magnetic flux with the pre-existing ambient field [54-61] or to the self-interaction of the bipolar EFRs [62]. Magnetic reconnection can supply enough energy to heat and accelerate the plasma in a complex

three-dimensional geometry. The energetics of the process is linked to the relative orientation between the emerging and pre-existing field lines [63].

Despite these advances in our knowledge about interactions between EFRs and ambient magnetic fields, there are still some open questions. In particular, we do not understand why small-energy release phenomena are not always observed in the EFRs.

Here, we present an analysis based on joint observations performed by the IRIS and SDO satellites, showing the evolution of an EFR embedded in the plage of the following polarity of AR NOAA 12529 [64,65]. This study revealed the phenomena occurring in the upper atmosphere during the photospheric evolution of the EFR, observing long-lasting intensity enhancements, similar to UV bursts, with simultaneous plasma ejections.

2. – Observations

The EFR analyzed in this work was observed in the plage field of the following polarity of AR NOAA 12529 (see the solid box in fig. 1). This AR, appeared on the solar disk during April 2016, was characterized by a β-type magnetic configuration, *i.e.*, a bipolar configuration except for the umbral filament observed in the leading sunspot with opposite polarity (see fig. 1, [66, 67]). Between April 13 and 14 it approached the central solar meridian, being located at heliocentric angle $\mu \approx 0.96$.

The IRIS satellite acquired three different data sets during the EFR evolution. In our study, we analyzed the observing sequence acquired between 22:34:43 UT on April 13 and 01:55:29 UT on April 14, consisting of six large dense 64-step raster scans. UV spectra were acquired in seven spectral ranges, which include, at increasing formation heights from the chromosphere up to the corona, the O I 1355.6 Å, Mg II h and k, C II 1334.5 and 1335.7 Å, Si IV 1394 and 1402 Å, and Fe XII 1349.4 Å lines. The exposure time was 30 s until exposure 10 in the second raster, then the automatic exposure control reduced it to 9 s for the near-UV channel and to 18 s for the far-UV channels, respectively. Such relatively long exposure times ensured a good signal-to-noise ratio for faint lines as well.
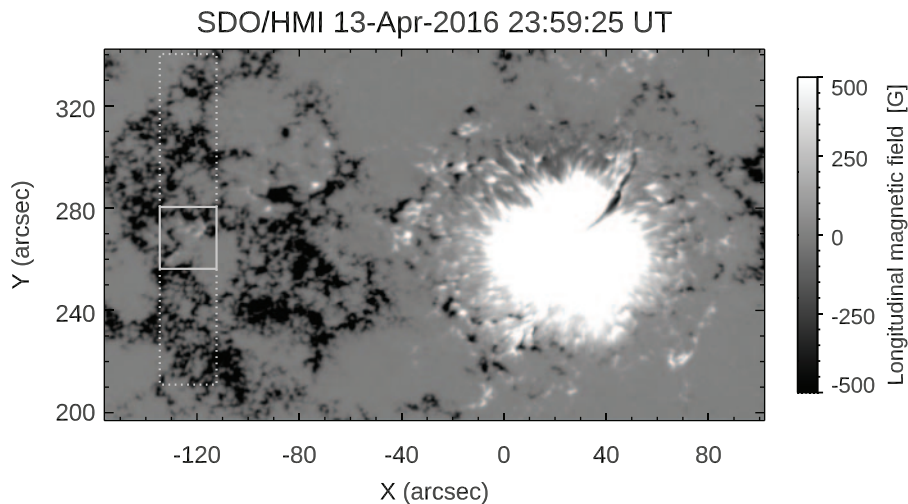

Fig. 1. – AR NOAA 12529 as seen in the SDO/HMI magnetogram at 23:59:25 UT, during the IRIS observations. The solid box frames the portion of the FoV where the EFR appears. The dashed box indicates the area covered by the IRIS slit during the six large dense 64-step rasters. Here and in the following figures, solar North is at the top, West is to the right.

Each scan had a $0\rlap{.}''33$ step size and a 31.5 s step cadence, with a pixel size of $0\rlap{.}''35$ along the y-direction. The cadence for an entire raster scan was about 33 min, covering a FoV of $22\rlap{.}''2 \times 128\rlap{.}''4$, as indicated in fig. 1 (dashed box). Simultaneously, Slit-Jaw Images (SJIs) were acquired in the 2796 and 1400 Å passbands, with temperature formation of about 10^4 K and 6.5×10^4 K, respectively. These SJIs have a cadence of 63 s for consecutive frames in each passband, covering a field of view (FoV) of $143\rlap{.}''7 \times 128\rlap{.}''4$. For further details about this data set and its analysis, we refer the reader to [64, 65].

We used photospheric observations from the SDO satellite to determine the context of IRIS observations. These data are full-disk continuum filtergrams and line-of-sight (LoS) magnetograms taken by the Helioseismic and Magnetic Imager (HMI, [68]) along the Fe 1 6173 Å line, with a spatial resolution of $1''$ and a cadence of 45 s. Images from the 131, 193, 171, 304, and 1600 Å filters acquired by the Atmospheric Imaging Assembly (AIA, [69]) were also considered in the present work. These EUV/UV data have a cadence of 12/24 s, respectively, and an image spatial scale of about $0\rlap{.}''6$ per pixel.

We aligned SDO/HMI continuum filtergrams to SDO/AIA data, which are already aligned between them, considering the different pixel size. Cross-correlation techniques were applied to align simultaneous IRIS and SDO observations, using the cospatial sub-FoV between the SDO/HMI continuum filtergrams and the integrated radiance in the IRIS 2832 Å band for each IRIS scan as a reference. The accuracy of the alignment is $\pm 0\rlap{.}''5$, a value that is comparable to the pixel size of SDO/HMI data.

3. – Results

Figure 1 displays that the EFR emerged in the trailing polarity of AR NOAA 12529, in a magnetic environment characterized by a unipolar configuration.

The sequence acquired by SDO/HMI, relative to the photospheric evolution of the EFR, indicates that before the emergence there was a pore at the center of the subFoV marked with a solid box in fig. 1, corresponding to a flux patch with positive polarity. This pore started to shrink when the corresponding positive flux patch got in contact with the emerging negative polarity of the EFR, decreasing in size as long as the new flux was emerging. Eventually, the pore disappeared and a new pore appeared, formed by the accumulation of newly emerged negative polarity flux brought by the EFR (see [64] for more details).

IRIS observations show repeated brightness enhancements in the EFR site. We clearly see a compact UV burst near the center of these images, within the subFoV where the EFR appeared (fig. 2, top panels). The UV burst, with a size of about $5'' \times 5''$, was observed throughout the IRIS observing sequence (more than three hours), appearing to consist of many transient and very dynamic sub-structures.

Light curves derived from the EUV/UV SDO/AIA data (193 Å and 1600 Å) and from IRIS SJIs in the 1400 Å passband were also computed, as shown in fig. 2 (bottom panel). For this analysis, we considered the common sub-FoV between the area scanned by the IRIS slit and the region where the EFR appeared in the SDO/HMI magnetograms. The largest variation in brightness occurred in the IRIS 1400 Å passband, which shows a strong increase during the third IRIS scan, followed by a peak and subsequent bursty behaviour. However, intensity enhancements are also seen in the 1600 Å and 193 Å SDO/AIA channels at the beginning of the third IRIS scan. Then, the 1600 Å intensity shows a smooth decrease until the end of the IRIS observations, while the 193 Å channel exhibits a more bursty trend. Indeed, SDO/AIA filtergrams show coronal brightening at the location of the UV burst throughout the IRIS observations (see [64, 65]).
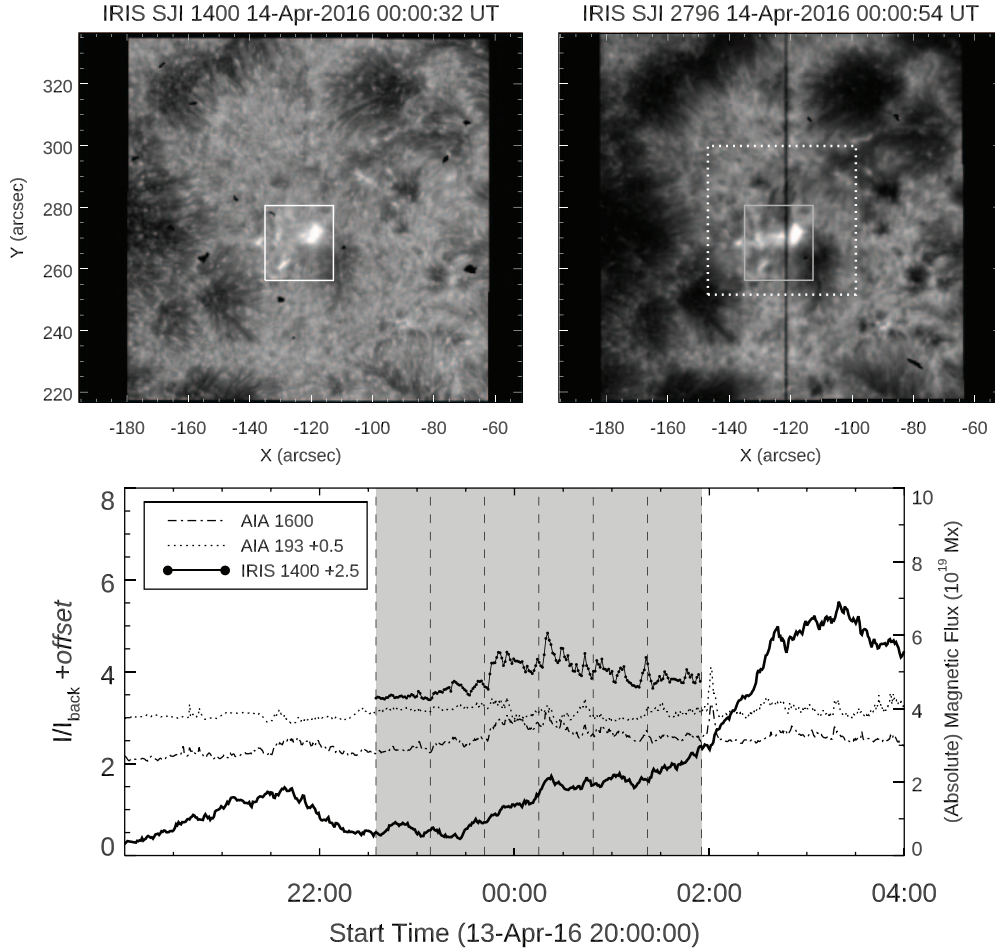
Fig. 2. – Top panels: IRIS SJI 1400 Å and 2796 Å co-temporal images relevant to the third raster scan of the analyzed sequence. The solid box marks the area scanned by IRIS, cospatial to the region where the EFR appears (solid box in fig. 1). The dashed line box indicates relevant to the eruption analyzed in fig. 3. Bottom panel: light curves as obtained from the SDO/AIA 1600 Å and 193 Å images and IRIS SJI 1400 Å in the above-mentioned region of flux emergence, indicated with a solid box. The grey-shaded area indicates the time interval of the IRIS rasters, specifying start and end times with dashed vertical lines. The trend of the negative magnetic flux in the EFR is also plotted (black thick line).

For comparison, the plot in fig. 2 (bottom panel) also displays the amount of negative magnetic flux emerging in the EFR (black thick line). Brightness enhancements occurred during the increase phase of the negative emerging flux. We notice that major intensity peaks took place a few minutes after steeper magnetic flux increments.

Plasma ejections also occurred during the evolution of the EFR. Several surge-like events are observed at chromospheric level, appearing as dark filamentary elongating structures, up to maximum length of ≈ 20 Mm. Jet-like dark features departing from the EUV brightening site are also seen in the simultaneous SDO/AIA images [64].

In addition, we studied the surge activity above the chromospheric arch filament system overlying the EFR using radiance maps deduced for the Si IV 1402 Å and Mg II k

2986.3 Å lines. Surges were detected in the Si IV 1402 Å line for the first time, likely owing to the effect of nonequilibrium ionization [61]. Comparing the UV emission in the blue and red wings of each line, we found that there are differences in the location of the emitting regions between the wings. This asymmetry can be explained taking into account the LoS effects: the ejected plasma, previously showing a blueshift, later falls back down, thus being redshifted, as suggested by numerical experiments [59-61].

The analysis of IRIS UV spectra suggests the occurrence of heating of dense plasma in the low solar atmosphere, up to $\approx 10^5$ K, as well as indicates the presence of bi-directional high-speed flows with velocity up to $\pm 150\,\mathrm{km\,s^{-1}}$ at the location of the UV burst.

Line profiles relevant to the UV burst core show typical blueshifts of about $50\,\mathrm{km\,s^{-1}}$, but also exhibit multi-peaked non-Gaussian profiles pointing to unresolved plasma components with different velocity in the same pixel. Line widths reach values of about $\pm 150\,\mathrm{km\,s^{-1}}$, indicating the presence of high-speed flows along opposite directions. The absence of emission in the O IV 1401.2 Å line is highly suggestive of a plasma density larger than $10^{12}\,\mathrm{cm^{-3}}$ and, together with the presence of the Mg II 2799 Å core triplet emission, implies that the reconnection event occurs at low chromospheric level.

A further characteristic observed in the UV burst core is the unexpected behaviour of the relative ratio between the intensities O I 1355.6 Å and C I 1355.8 Å lines. The latter is a factor of two stronger than the O I line, as usually observed during flares. This might be caused by electron density increase, but theoretical confirmation is needed.

Interestingly, the detection of a signal above the background in the forbidden Fe XII 1349 Å, with temperature formation of $\log T$ [K] ≈ 6.2, reveals that plasma in the reconnection site is heated up to temperatures of this order of magnitude [65]. This might explain the brightening seen in the SDO/AIA coronal channels, cospatial to the UV burst, as being due to plasma heated up to coronal temperatures.

Therefore, the UV burst occurs somewhere in the low atmosphere, and the reconnection involves all the solar atmospheric layers. The location of the reconnection site and the magnetic topology are likely responsible for the observed eruptive phenomena.

The preliminary results of the late evolution of the EFR reveal an even more dramatic scenario, with violent eruptions and flaring.

A few minutes after the end of IRIS observations, a sudden intensity peak is observed in the SDO/AIA light curves, being simultaneous in all of the EUV/UV channels (see, *e.g.*, fig. 2, bottom panel). The X-ray flux measured by the GOES satellite indicates that at 01:56 UT a flare of class B7.4 occurred.

Figure 3 illustrates the development of the eruption that is observed soon after the peak of the B7.4 flare. The panels of fig. 3 show SDO/AIA filtergrams at decreasing temperature formation heights, from the corona (131 Å) down to the chromosphere/upper photosphere (304 Å and 1600 Å). The formation of a circular flare ribbon is clearly detected (see fig. 3, second and third rows). This occurs in a fan-spine magnetic topology due to the presence parasitic polarities [70, 71], as is the case in our observations, with the negative emerging polarity of the EFR embedded in the unipolar positive-polarity field of the plage of the trailing polarity of AR NOAA 12529.

Furthermore, a few minutes after the occurrence of the eruption, coronal plasma appears to undergo catastrophic cooling (see fig. 3, fifth and sixth rows). This process is characterized by a rapid fall in coronal temperature, with a subsequent change in the coronal density leading to the formation of cool condensations. As a result, a previously emitting structure suddenly darkens and dense blobs fall down to the lower atmosphere.

These findings are reminiscent of the results obtained in numerical experiments of flux emergence, which show the launching of a hot and fast coronal jet followed by
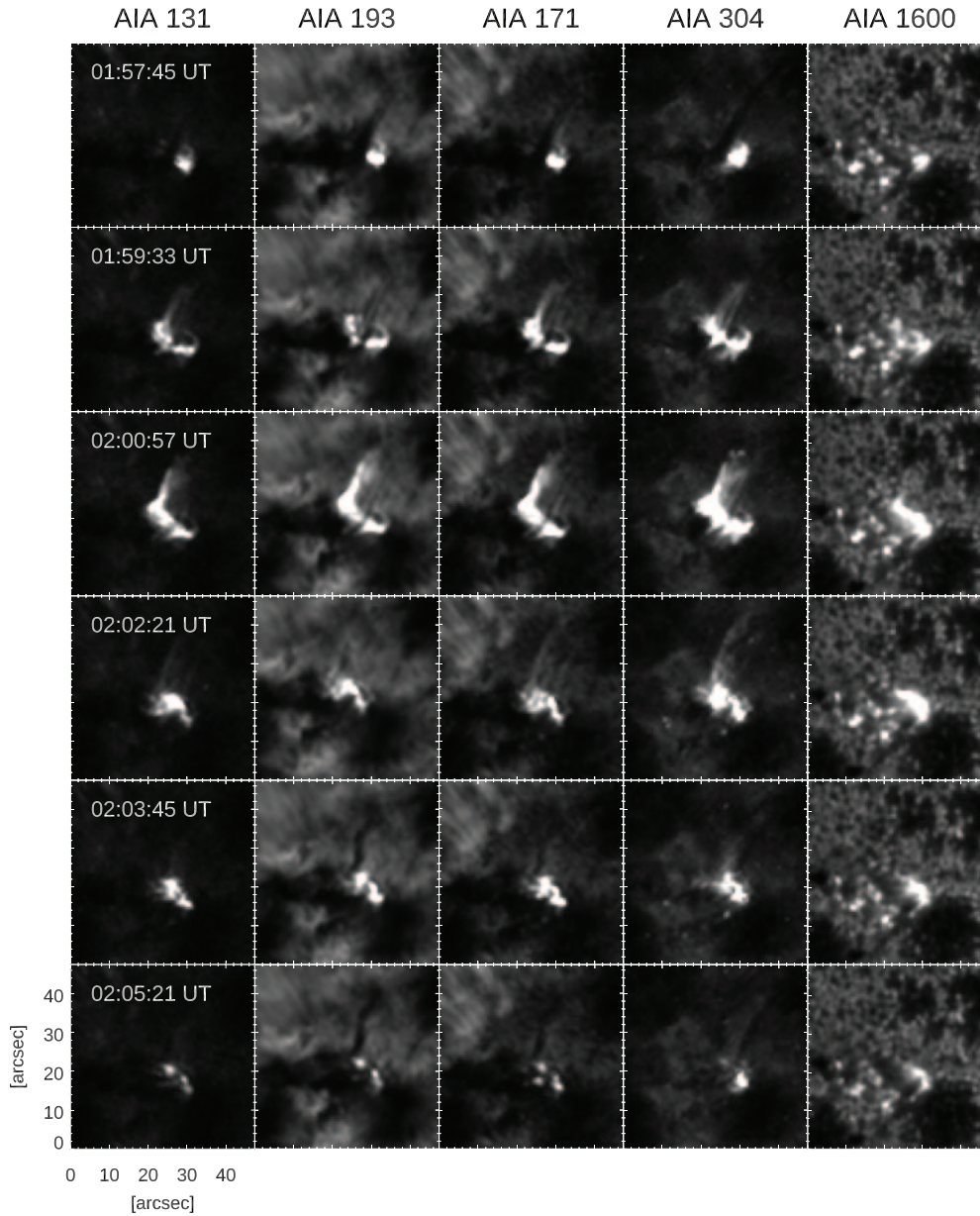
Fig. 3. – Sequence of SDO/AIA filtergrams showing the evolution at different atmospheric heights of the eruption occurring after the B7.4 flare at 01:56 UT on April 14, with a ≈ 1.5 minutes cadence. SDO/AIA filtergrams are shown at decreasing temperature formation heights.

several violent eruptions during the decay phase, resembling mini-CMEs [72]. These reconnection events can be followed by radiative thermal instability causing catastrophic cooling [73].

The characterization of these events occurring during the late emergence phases will be the subject of a follow-up paper, currently in preparation.
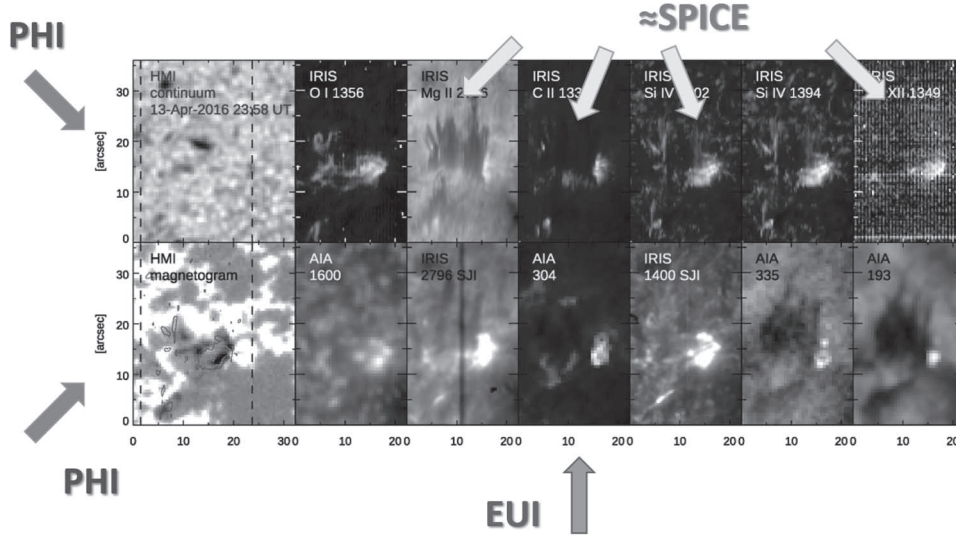
Fig. 4. – Synoptic view of the EFR area at different atmospheric layers from simultaneous multi-wavelength measurements of IRIS, SDO/HMI and SDO/AIA, acquired during the third IRIS scan. The overplotted contours on the LoS magnetogram refer to the Si IV 1402 Å radiance. Potential targets for observations using remote-sensing instruments aboard the SolO spacecraft are indicated.

4. – Conclusions

In this work, we have found evidence for a small-scale EFR showing a significant impact in the upper atmospheric layers.

Photospheric observations indicate that cancellation of pre-existing flux occurs as a consequence of flux emergence in a unipolar plage. A pre-existing pore, with positive polarity, slowly vanishes being replaced by a new pore characterized by opposite polarity, formed by the piling up of the negative emerging flux. Recurrent chromospheric brightening and a UV burst, with counterparts in the corona, are simultaneously observed throughout the flux emergence process. High-speed plasma flows are recognized in the signature of surge/jet-like activity both in images and spectra. At the late phases of flux emergence, eruption and flaring occur, with a fan-spine topology.

These findings suggest that the interplay between emerging fields and other flux systems triggers energy release phenomena through small-scale magnetic reconnection episodes taking place in the low chromosphere.

A significant advance in our understanding of magnetic reconnection during flux emergence will be possible with upcoming high-resolution, multi-wavelength observations performed by the Solar Orbiter (SolO, [74]) space mission. In fig. 4 we display a synoptic view of the event studied in this work as a suggestion for future observations. Arrows indicate the target for the remote-sensing instruments of the Solar Orbiter spacecraft that can be potentially involved in the investigation of these small-scale reconnection events. SolO/PHI [75] will provide photospheric continuum images and magnetograms, while simultaneous SolO/EUI [76] and SolO/SPICE [77] observations will allow us to obtain imaging and spectroscopic information for the chromosphere and corona.

* * *

REFERENCES

[1]   Charbonneau P., *Living Rev. Sol. Phys.*, **17** (2020) 4.
[2]   Parker E. N., *Astrophys. J.*, **121** (1955) 491.
[3]   Fan Y., *Living Rev. Sol. Phys.*, **6** (2009) 4.
[4]   van Driel-Gesztelyi L. and Green L. M., *Living Rev. Sol. Phys.*, **12** (2015) 1.
[5]   Solanki S. K., *Astron. Astrophys. Rev.*, **11** (2003) 153.
[6]   Bellot Rubio L. and Orozco Suárez D., *Living Rev. Sol. Phys.*, **16** (2019) 1.
[7]   Kosugi T., Matsuzaki K., Sakao T. *et al.*, *Sol. Phys.*, **243** (2007) 3.
[8]   Pesnell W. D., Thompson B. J. and Chamberlin P. C., *Sol. Phys.*, **275** (2012) 3.
[9]   Martínez Pillet V., Del Toro Iniesta J. C., Álvarez-Herrero A. *et al.*, *Sol. Phys.*, **268** (2011) 57.
[10] Solanki S. K., Barthol P., Danilovic S. *et al.*, *Astrophys. J. Lett.*, **723** (2010) L127.
[11] Solanki S. K., Riethmüller T. L., Barthol P. *et al.*, *Astrophys. J. Suppl. Ser.*, **229** (2017) 2.
[12] Barthol P., Gandorfer A., Solanki S. K. *et al.*, *Sol. Phys.*, **268** (2011) 1.
[13] Danilovic S., Beeck B., Pietarila A. *et al.*, *Astrophys. J. Lett.*, **723** (2010) L149.
[14] Guglielmino S. L., Martínez Pillet V., Bonet J. A. *et al.*, *Astrophys. J.*, **745** (2012) 160.
[15] Palacios J., Blanco Rodríguez J., Vargas Domínguez S. *et al.*, *Astron. Astrophys.*, **537** (2012) A21.
[16] Guglielmino S. L., Martínez Pillet V., Ruiz Cobo B. *et al.*, *Astrophys. J.*, **896** (2020) 62.
[17] Lagg A., Solanki S. K., Riethmüller T. L. *et al.*, *Astrophys. J. Lett.*, **723** (2010) L164.
[18] Martínez González M. J., Bellot Rubio L. R., Solanki S. K. *et al.*, *Astrophys. J. Lett.*, **758** (2012) L40.
[19] Gandorfer A., Grauf B., Barthol P. *et al.*, *Sol. Phys.*, **268** (2011) 35.
[20] Centeno R., Blanco Rodríguez J., Del Toro Iniesta J. C. *et al.*, *Astrophys. J. Suppl. Ser.*, **229** (2017) 3.
[21] Kaithakkal A. J, and Solanki S. K., *Astron. Astrophys.*, **622** (2019) A200.
[22] De Pontieu B., Title A. M., Lemen J. R. *et al.*, *Sol. Phys.*, **289** (2014) 2733.
[23] Huang Z., Madjarska M. S., Xia L. *et al.*, *Astrophys. J.*, **797** (2014) 88.
[24] Gupta G. R. and Tripathi D., *Astrophys. J.*, **809** (2015) 82.
[25] Huang Z., Madjarska M. S., Scullion E. M. *et al.*, *Mon. Not. R. Acad. Sci.*, **464** (2017) 1753.
[26] Tian H., Kleint L., Peter H. *et al.*, *Astrophys. J. Lett.*, **790** (2014) L29.
[27] Vissers G. J. M., Rouppe van der Voort L. H. M. and Carlsson M., *Astrophys. J. Lett.*, **811** (2015) L33.
[28] Bai X. Y., Su J. T., Cao W. D. *et al.*, *Astrophys. J.*, **823** (2016) 60.

[29] SAMANTA T., TIAN H., BANERJEE D. and SCHANCHE N., *Astrophys. J. Lett.*, **835** (2017) L19.

[30] MURABITO M., GUGLIELMINO S. L., ERMOLLI I. *et al.*, *Astrophys. J.*, **890** (2020) 96.

[31] PETER H., TIAN H., CURDT W. *et al.*, *Science*, **346** (2014) 1255726.

[32] YOUNG P. R., TIAN H., PETER H. *et al.*, *Space Sci. Rev.*, **214** (2018) 120.

[33] GRUBECKA M., SCHMIEDER B., BERLICKI A. *et al.*, *Astron. Astrophys.*, **593** (2016) A32.

[34] TIAN H., XU Z., HE J. and MADSEN C., *Astrophys. J.*, **824** (2016) 96.

[35] CHITTA L. P., PETER H., YOUNG P. R., and HUANG Y.-M., *Astron. Astrophys.*, **605** (2017) A49.

[36] HONG J., DING M. D. and CAO W., *Astrophys. J.*, **838** (2017) 101.

[37] ROUPPE VAN DER VOORT L., DE PONTIEU B., SCHARMER G. B. *et al.*, *Astrophys. J. Lett.*, **851** (2017) L6.

[38] ZHAO J., SCHMIEDER B., LI H. *et al.*, *Astrophys. J.*, **836** (2017) 52.

[39] TIAN H., ZHU X., PETER H. *et al.*, *Astrophys. J.*, **854** (2018) 174.

[40] PRIEST E. and FORBES T., *Magnetic Reconnection* (Cambridge University Press, Cambridge) 2000, p. 612.

[41] BENZ A. O., *Living Rev. Sol. Phys.*, **14** (2017) 2.

[42] SHIMIZU T., *Phys. Plasmas*, **22** (2015) 101207.

[43] GUGLIELMINO S. L., in *Proceedings of the 4th Hinode Science Meeting: Unsolved Problems and Recent Insights* Vol. **455** (2012) p.109.

[44] GUGLIELMINO S. L., ZUCCARELLO F., ROMANO P. and BELLOT RUBIO L. R., *Astrophys. J. Lett.*, **688** (2008) L111.

[45] GUGLIELMINO S. L., BELLOT RUBIO L. R., ZUCCARELLO F. *et al.*, *Astrophys. J.*, **724** (2010) 1083.

[46] VARGAS DOMÍNGUEZ S., VAN DRIEL-GESZTELYI L., and BELLOT RUBIO L. R., *Sol. Phys.*, **794** (2014) 140.

[47] VARGAS DOMÍNGUEZ S., KOSOVICHEV A. and YURCHYSHYN V., *Astrophys. J.*, **794** (2014) 140.

[48] ORTIZ A., BELLOT RUBIO L. R., HANSTEEN V. H. *et al.*, *Astrophys. J.*, **781** (2014) 126.

[49] DE LA CRUZ RODRÍGUEZ J., HANSTEEN V., BELLOT-RUBIO L. and ORTIZ A., *Astrophys. J.*, **810** (2015) 145.

[50] ORTIZ A., HANSTEEN V. H., BELLOT RUBIO L. R. *et al.*, *Astrophys. J.*, **825** (2016) 93.

[51] TORIUMI S., KATSUKAWA Y. and CHEUNG M. C. M., *Astrophys. J.*, **836** (2017) 63.

[52] ORTIZ A., HANSTEEN V. H., NÓBREGA-SIVERIO D. and ROUPPE VAN DER VOORT L., *Astron. Astrophys.*, **633** (2020) A58.

[53] YOKOYAMA T. and SHIBATA K., *Nature*, **375** (1995) 42.

[54] ARCHONTIS V. and HOOD A. W., *Astron. Astrophys.*, **508** (2009) 1469.

[55] MACTAGGART D., GUGLIELMINO S. L., HAYNES A. L. *et al.*, *Astron. Astrophys.*, **576** (2015) A4.

[56] SYNTELIS P., ARCHONTIS V., GONTIKAKIS C. and TSINGANOS K., *Astron. Astrophys.*, **584** (2015) A10.

[57] NI L., KLIEM B., LIN J. and WU N., *Astrophys. J.*, **799** (2015) 79.

[58] NI L., LIN J. ROUSSEV I. I. and SCHMIEDER B., *Astrophys. J.*, **832** (2016) 195.

[59] NÓBREGA-SIVERIO D., MORENO-INSERTIS F. and MARTÍNEZ-SYKORA J., *Astrophys. J.*, **822** (2016) 18.

[60] NÓBREGA-SIVERIO D., MARTÍNEZ-SYKORA J., MORENO-INSERTIS F. and ROUPPE VAN DER VOORT L., *Astrophys. J.*, **850** (2017) 153.

[61] NÓBREGA-SIVERIO D., MORENO-INSERTIS F. and MARTÍNEZ-SYKORA J., *Astrophys. J.*, **858** (2018) 8.

[62] HANSTEEN V. H., ARCHONTIS V., PEREIRA T. M. D. *et al.*, *Astrophys. J.*, **839** (2017) 22.

[63] GALSGAARD K., ARCHONTIS V., MORENO-INSERTIS F. and HOOD A. W., *Astrophys. J.*, **666** (2007) 516.

[64] GUGLIELMINO S. L., ZUCCARELLO F., YOUNG P. R. *et al.*, *Astrophys. J.*, **856** (2018) 127.

[65] GUGLIELMINO S. L., YOUNG P. R. and ZUCCARELLO F., *Astrophys. J.*, **871** (2019) 82.

[66] Guglielmino S. L., Romano P. and Zuccarello F., *Astrophys. J. Lett.*, **846** (2017) L16.
[67] Guglielmino S. L., Romano P., Ruiz Cobo B. *et al.*, *Astrophys. J.*, **880** (2019) 34.
[68] Scherrer P. H., Schou J., Bush R. I. *et al.*, *Sol. Phys.*, **275** (2012) 207.
[69] Lemen J. R., Title A. M., Akin D. J. *et al.*, *Sol. Phys.*, **275** (2012) 17.
[70] Masson S., Pariat E., Aulanier G. and Schrijver C. J., *Astrophys. J.*, **700** (2009) 559.
[71] Romano P., Falco M., Guglielmino S. L. and Murabito M., *Astrophys. J.*, **837** (2017) 173.
[72] Moreno-Insertis F. and Galsgaard K., *Astrophys. J.*, **771** (2013) 20.
[73] Xia C., Keppens R. and Fang X., *Astron. Astrophys.*, **603** (2017) A42.
[74] Müller D., St. Cyr O. C., Zouganelis I. *et al.*, *Astron. Astrophys.*, **642** (2020) A1.
[75] Solanki S. K., del Toro Iniesta J. C., Woch J. *et al.*, *Astron. Astrophys.*, **642** (2020) A11.
[76] Rochus P., Auchère F., Berghmans D. *et al.*, *Astron. Astrophys.*, **642** (2020) A8.
[77] Spice Consortium, Anderson M., Appourchaux T. *et al.*, *Astron. Astrophys.*, **642** (2020) A14.